The Astrophysical Journal, 696:160–171, 2009 May 1 doi:10.1088/0004-637X/696/1/160

VARIABLE PARTIAL COVERING AND A RELATIVISTIC IRON LINE IN NGC 1365

G. Risaliti[1,2], G. Miniutti[3], M. Elvis[1], G. Fabbiano[1], M. Salvati[2], A. Baldi[1], V. Braito[4,5], S. Bianchi[6], G. Matt[6], J. Reeves[7], R. Soria[8], and A. Zezas[1]

[1] Harvard-Smithsonian Center for Astrophysics, 60 Garden St. Cambridge, MA 02138, USA; grisaliti@cfa.harvard.edu
[2] INAF-Osservatorio di Arcetri, Largo E. Fermi 5, I-50125 Firenze, Italy
[3] Laboratoire Astroparticule et Cosmologie (APC), UMR 7164, 10 Rue A. Domon et L. Duquet, 75205 Paris, France
[4] Department of Physics and Astronomy, University of Leicester, University Road, Leicester LE1 7RH, UK
[5] Department of Physics and Astronomy, Johns Hopkins University, Baltimore, MD 21218, USA
[6] Dipartimento di Fisica, Università degli Studi "Roma Tre," Via della Vasca Navale 84, I-00146 Roma, Italy
[7] Astrophysics Group, School of Physical and Geographical Science, Keele University, Keele, Staffordshire ST5 5BG, UK
[8] MSSL, University College London, Holmbury St. Mary, Dorking, Surrey RH5 6NT, UK
Received 2008 July 28; accepted 2009 January 27; published 2009 April 14

ABSTRACT

We present a complete analysis of the hard X-ray (2–10 keV) properties of the Seyfert galaxy NGC 1365, based on a 60 ks *XMM-Newton* observation performed in 2004 January. The two main results are as follows. (1) We detect an obscuring cloud with $N_H \sim 3.5 \times 10^{23}$ cm^{-2} crossing the line of sight in ∼25 ks. This implies a dimension of the X-ray source not larger than a few 10^{13} cm and a distance of the obscuring cloud of the order of 10^{16} cm. Adopting the black hole mass $M_{\rm BH}$ estimated from the $M_{\rm BH}$–velocity dispersion relation, the source size is $D_{\rm S} < 20R_G$ and the distance and density of the obscuring clouds are $R \sim 3000$–$10{,}000R_G$ and $n \sim 10^{10}$ cm^{-3}, i.e., typical values for broad-line region clouds. (2) An iron emission line with a relativistic profile is detected with high statistical significance. A time-integrated fit of the line+continuum reflection components suggests a high iron abundance (approximately three times solar) and an origin of these components in the inner part (within $\sim 10R_G$) of the accretion disk, in agreement with the small source size inferred from the analysis of the absorption variability.

Key words: galaxies: active – galaxies: individual (NGC 1365) – X-rays: galaxies

Online-only material: color figures

1. INTRODUCTION

According to the unified model of active galactic nuclei (AGNs; see review by Urry & Padovani 1995), an axisymmetric absorber/reflector is present around the central black hole of AGNs, with a size between that of the broad emission line region (BELR; ∼ 1000 Schwarzschild radii) and that of the narrow-line region (tens to hundreds of parsecs). The easiest geometrical and physical configuration of such absorber is that of a homogeneous torus on a parsec scale (Krolik & Begelman 1988). However, this view has been recently challenged by several pieces of observational evidence.

1. Dramatic X-ray absorbing column density changes (factors of >10) over a few years have been seen in several type 2 (narrow permitted lines) Seyferts (Risaliti et al. 2002), ruling out a homogeneous absorber.
2. Rapid column density variability, on timescales of hours, requires an X-ray absorber no larger than the BELR. Such changes have been detected in the brightest absorbed Seyfert galaxy, NGC 4151 (∼10–30 hr; Puccetti et al. 2007) and in the Seyfert 2 galaxy NGC 4388 (4 hr; Elvis et al. 2004). Assuming that the absorber is made by material moving with Keplerian velocity around the central source, these observations imply that its distance is of the order of the broad-line clouds, i.e., a small fraction of a parsec. In order to have the absorber at a parsec from the center, the linear size of the clouds should be of the order of 10^{11} cm, much smaller than the minimum possible size of the X-ray source (at least ∼ 10 gravitational radii, i.e., several 10^{12} cm for a 10^7 $M_\odot$ black hole).
3. An indication of strong inhomogeneities in the absorber/reflector comes from the analysis of the reflection components in the X-ray spectra of Compton-thin Seyfert Galaxies, which are systematically stronger than expected from reflection by gas with the same column density as measured in absorption. This has been shown convincingly for a few sources in which a detailed measurement of the reflection component has been possible (NGC 1365, Risaliti et al. 2000; NGC 2992, Gilli et al. 2000; NGC 6300, Guainazzi 2002) and in a statistical sense in a sample of ∼20 bright Seyfert 2s (Risaliti 2002). This implies the presence of Compton-thick reflecting material out of the line of sight, and covering a significant fraction of the solid angle as seen from the X-ray source (Ghisellini et al. 1994; Magdziarz & Zdziarski 1995).

Here we report on a 60 ks *XMM-Newton* observation of the obscured AGN in NGC 1365, which put new stronger constraints on the size and structure of its circumnuclear absorber.

The same observation also revealed a prominent broad iron emission line with a relativistic profile. Asymmetric profiles of iron-Kα emission lines are one of the possible probes of the extreme general relativistic effects around black holes. This issue has been thoroughly investigated in the past 15–20 years both from a theoretical and an observational point of view. The iron emission from an accretion disk around a black hole has been modeled taking into account the broadening and Doppler boosting due to the disk rotation, and the gravitational redshift due to the black hole field (Fabian et al. 1989). Several models predict the line profile from a maximally rotating black hole (e.g., Laor 1991; Dovčiak et al. 2004), considering different emissivity profiles, emitting regions, disk ionization states, and viewing angles (for a review, see Fabian & Miniutti 2009). Observationally, the asymmetric profile attributed to the relativistic line has been first observed by *ASCA* in MCG-6-30-15

(Tanaka et al. 1995), and subsequently in several AGNs and Galactic black holes with *ASCA*, *BeppoSAX*, *XMM-Newton*, and *Suzaku* (e.g., Miller 2007; Nandra et al. 2007)

The main open issue in this field is due to the large width of the relativistically broadened line, extending from the peak energy around 6–7 keV down to 3–5 keV in the most extreme cases, depending on the disk parameters. Such a broad feature can be effectively mimicked by continuum curvatures, due to reflection components, partial covering by circumnuclear gas, or to a poor determination of the intrinsic continuum (usually modeled with a simple power law). Recently, Miller et al. (2008) showed that it is formally possible to reproduce the X-ray spectrum of MCG-6-30-15, with its broad emission feature (which is so far the highest quality relativistic line candidate) through a model which includes a warm absorber with a variable partial covering of the central source.

Here, we show that the identification of the broad feature in the *XMM-Newton* spectrum of NGC 1365 as a relativistically broadened iron-K line is rather solid, thanks to a combination of favorable aspects: a high iron metallicity, which implies a large equivalent width of the line, and a sharp low-energy tail, which is impossible to reproduce with partial-covering scenarios.

2. THE X-RAY OBSERVATIONAL HISTORY OF NGC 1365

NGC 1365 ($z = 0.0055$) is a particularly striking example of absorption variability. It was observed by *ASCA* in 1995 in a reflection-dominated state ($N_H > 10^{24}$ cm^{-2}; Iyomoto et al. 1997) and, three years later, in a Compton-thin state ($N_H \sim 4 \times 10^{23}$ cm^{-2}) by *BeppoSAX* (Risaliti et al. 2000). The ratio between the 2 and 10 keV flux of the reflected component and that of the intrinsic spectrum was higher than 5%. Such a high reflection efficiency can be achieved only if a thick ($N_H > 3 \times 10^{24}$ cm^{-2}) reflector covers a large fraction of the solid angle around the central source (Ghisellini et al. 1994; Magdziarz & Zdziarski 1995).

The switch from reflection-dominated to Compton-thin states could in principle be due either to extreme variations of the intrinsic luminosity (Matt et al. 2003) or to Compton-thick clouds moving across the line of sight.

In order to resolve the uncertainty between these two physical explanations, and to study the complex structure of the circumnuclear material, NGC 1365 was observed many times with *XMM-Newton* and *Chandra* in the past few years, revealing a series of unique properties.

1. The X-ray obscuration varies dramatically. We first found two Compton-thick to Compton-thin transitions in a series of three *Chandra* and *XMM-Newton* snapshot observations performed in a total period of 6 weeks (Risaliti et al. 2005b, hereafter R05B). We then performed a *Chandra* monitoring campaign consisting of six short (10 ks) observations in 10 days, which revealed changes from reflection-dominated to transmission-dominated spectra on a timescale shorter than 2 days (Risaliti et al. 2007). This fast variability completely rules out the intrinsic variability scenario, leaving occultation by a circumnuclear cloud as the only plausible cause of the observed variations.
2. A series of four *XMM-Newton* observations, during which the source was in a Compton-thin state, revealed a complex of absorption lines, detected with high statistical significance, at energies between 6.7 and 8 keV (Risaliti et al. 2005a, hereafter R05A). These lines are due to Fe XXV and Fe XXVI Kα and Kβ resonant absorption by a highly ionized gas with column density of a few 10^{23} cm^{-2}, one of the most extreme warm absorbers (both for the high N_H and the high ionization state) detected so far among AGNs.
3. The soft thermal component which dominates below 2 keV is constant within 5% in all observations. The high spatial resolution of *Chandra* allowed us to resolve the emitting region, which extends over $\sim$ 1 kpc from the center, while the hard component originates in a region with diameter $<$100 pc (10 arcsec), as commonly observed in Seyfert Galaxies (Bianchi et al. 2006; Guainazzi & Bianchi 2007). The analysis of the *Chandra* observations of spatially diffused component is presented in a companion paper (Wang et al. 2009).

Table 1
NGC 1365—General Parameters

OBS	Counts	T [a]	F(2–10)[b]
Total	103907	60	1.37
INT 1	41784	22	1.39
INT 2	44362	26	1.20
INT 3	17761	12	1.42

Notes.
[a] Observing time, in ks.
[b] Observed 2–10 keV flux, in units of 10^{-11} erg s^{-1} cm^{-2}.

3. DATA REDUCTION

The observation was performed on 2004 January 18–19, with the EPIC PN and MOS instruments (Strüder et al. 2001; Turner et al. 2001) onboard the *XMM-Newton* observatory. Simultaneous Reflection Grating Spectrometer (RGS) spectra were also obtained. These data have been presented by Guainazzi & Bianchi (2007) and are not discussed in the present work. The data were reduced using the SAS package following the standard procedure suggested in the *XMM-Newton* manuals and threads.[9] The data were first checked for high background flares. No strong flare was present, so the whole exposure has been used in the analysis. The MOS event files were merged before the extraction of the scientific data. The PN data were treated separately.

Spectra and light curves were extracted from a 30 arcsec radius circular region around the nuclear source. The EPIC image is complex, showing an extended galactic emission and several individual galactic sources, but the nuclear source within 30 arcsec outshines the rest of the galaxy by a factor $>$30. The background was extracted from nearby regions (but outside the galaxy) in the same fields. The response files were created using the SAS package.

The same procedure has been repeated for all the subsequent extractions where time or energy filters have been applied (as we will show later, we extracted light curves in specific energy ranges, and spectra in many different time intervals). The relevant data about the spectra obtained from the whole observation, and from the different time intervals discussed in the next sections, are shown in Table 1.

4. DATA ANALYSIS: FULL OBSERVATION

The analysis of the spectra has been partially presented in a previous paper (R05A) where we focused on one single spectral

[9] http://xmm.esac.esa.int/sas/8.0.0/

feature: the presence of four iron absorption lines in the 6.7–8.3 keV spectral interval. Since these are narrow features, it was possible to investigate their properties without discussing the continuum fit in detail: any analytical fit correctly representing the continuum level at the lines' energy was acceptable.

Here we are instead interested in the physical properties of the 2–10 keV continuum and in broad features.

A second observation of similar length was performed six months later, and is also presented in R05A. We performed a complete analysis of these data, analogous to the one presented here. No significant spectral variability was detected during this observation. Moreover, due to the high measured column density ($N_H \sim 4 \times 10^{23}$ cm^{-2}) most of the iron line broad emission is obscured. For these reasons we do not discuss all the details of the data analysis. A summary of the relevant results is presented in Section 5.5.

The spectral analysis has been performed using the XSPEC 12.4 analysis package (Arnaud 1996). In all cases we used both the PN and MOS spectra. We normalized our fluxes to the MOS values. The PN normalizations are always consistent with those of MOS within <5%. All the parameters and errors quoted in this paper refer to simultaneous fits to both PN and MOS data. However, many of the figures contain PN data only, for the sake of clarity.

The model adopted in R05A consists of the following components:

1. a continuum power law absorbed by a column density $N_H \sim 2 \times 10^{23}$ cm^{-2},
2. a set of four absorption lines at energies between 6.7 and 8.3 keV, due to iron XXV and XXVI Kα and Kβ transitions,
3. a cold reflection component modeled through the PEXRAV model (Magdziarz & Zdziarski 1995),
4. an unabsorbed power law, with a normalization of a few percent of that of the main continuum component and the same photon index,
5. a broad FeK iron emission line, with a relativistic profile,
6. a narrow (unresolved) iron FeK emission line, at rest-frame energy $E = 6.39$ keV, and
7. an optically thin thermal component with $kT \sim 0.8$ keV, responsible for the bulk of the soft ($E < 2$ keV) emission.

In addition to the spectral components already listed, we also added a continuum from an ionized reflector (PEXRIV model in XSPEC). This component is needed to model a possible second screen located close to the source (e.g., the accretion disk itself), and therefore likely to be obscured when the source is in a Compton-thick state. Given the possible low distance from the central black hole of the ionized gas, we also allowed for relativistic blurring of this component. Specifically, we used the convolution model *kdblur* in XSPEC, developed by A. Fabian and R. Johnstone, which smoothes an arbitrary continuum according to the relativistic effects from an accretion disk around a maximally rotating black hole. The parameters of this component (inner and outer radii, and emissivity profile) are not tied to the corresponding parameters in the broad emission line component. This in principle allows for different emitting regions for the line and continuum components. Since in none of the fits presented in the following sections these parameters are significantly constrained, we do not discuss them in the intermediate steps of our analysis, and we link them to the broad emission line parameters in the final fit presented in Section 5.4.

The continuum reflection component (3) was initially frozen at the best value obtained from a previous *XMM-Newton* observation (OBS 2 in R05B) which caught the source in a Compton-thick, reflection-dominated state. This choice is based on the assumption that the reflection component remains constant on long timescales. This is the case if the distance of the cold reflector is large compared with the speed of light times the typical variability timescale. This hypothesis could not be verified with the data analyzed here. However, the fast absorption variability found with the *Chandra* campaign suggests that the absorber/reflector is located quite close to the central source (distance $<10^{16}$ cm; Risaliti et al. 2007). We will discuss possible variations of this component in the next sections. Here we are only interested in defining a baseline model to use as an initial step to develop our time-resolved analysis.

A complete analysis of the four iron absorption lines is presented in R05A and is not repeated in this paper. Here we only mention the results relevant for the present analysis.

1. The EW of the absorption lines is among the highest ever detected in AGNs (EW(Fe XXV Kα) $\sim$ 180 eV).
2. The lines are partially saturated. This implies that a global fit with ionized absorber models (e.g., through the XSTAR code) is not easily implemented. Instead, we analyzed the lines parameters, measured through Gaussian fits, with a model developed by Bianchi et al. (2005), which takes into account line saturation effects, the ionization state of the obscuring gas, and its turbulence velocity.
3. The result of our analysis is that absorber has an ionization parameter $U > 1000$,[10] and a column density $N_H \sim$ a few 10^{23} cm^{-2}.

In order to include possible effects of continuum absorption due to this gas, we used XSTAR to estimate the global effect of this warm absorber on the continuum emission. We find that, due to the high ionization state, no other significant alteration of the incident continuum (except for the iron absorption lines) is expected. Therefore, we always include the set of four absorption lines in all the fits presented here, with no further absorption component due to this gas.

The model consisting of the components summarized above provided a marginally acceptable fit ($\chi^2 = 1905/1752$ degrees of freedom (dof), Figure 1).

One of the most interesting features of this spectrum is the broad iron line (Figure 2). This component is well fitted with a profile produced by a maximally rotating black hole (LAOR model in XSPEC; Laor 1991), plus a narrow (unresolved) component. Interestingly, the best-fit flux of the narrow component is consistent with the flux measured in the purely reflection-dominated spectrum presented in R05B, suggesting a constancy of this component on long (several years) timescales.

We note that several residuals suggesting a nonoptimal continuum fit are apparent in Figures 1 and 2. This also implies that the interpretation of the broad feature in Figure 2 as a relativistic iron line has to be considered as tentative.

In principle, we could try to obtain better results adopting a more complex model, allowing for more absorption/reflection components. However, we will show in the following that this is not the right approach in this case, since most of the remaining deviations from a simple power law are due to absorption variability.

[10] Throughout this paper, the ionization parameter is defined as $U = L_X/(nR^2)$, where L_X is the ionizing X-ray luminosity and n_e is the number density of particles in the gas. U is therefore expressed in units of erg cm s^{-1}.

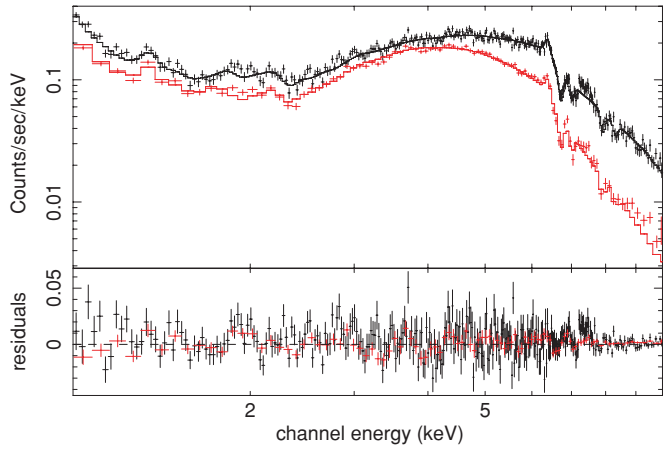

Figure 1. Data, best-fit model, and residuals for spectrum obtained from the whole 60 ks *XMM-Newton* observation. The baseline model described in the text, and first described in R05A, is adopted. Both PN and MOS data are plotted.

(A color version of this figure is available in the online journal.)

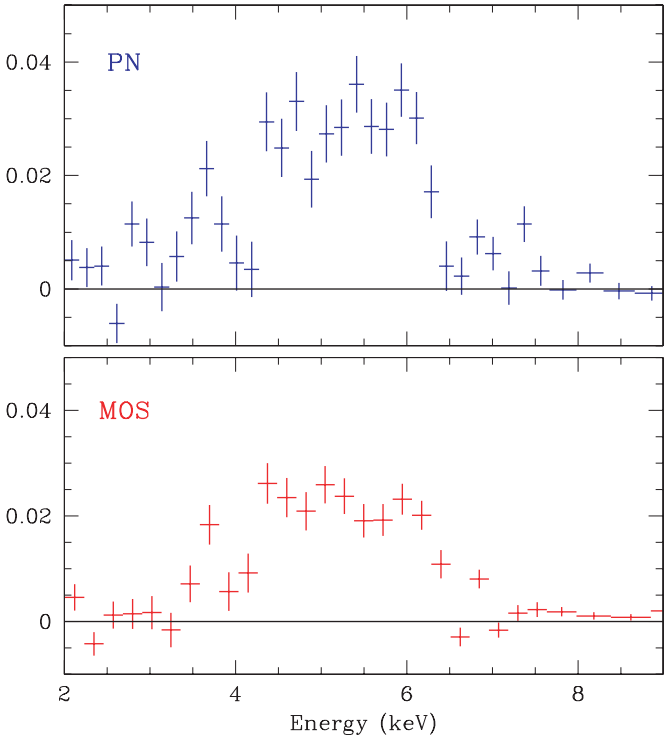

Figure 2. Residuals with respect to the best-fit continuum model (without the iron emission features) described in the text. Upper panel: PN instrument; lower panel: merged MOS. The fit was performed on the data without the 4–6.5 keV interval. These data were then renoted after the fit.

(A color version of this figure is available in the online journal.)

Here we start from the time-integrated analysis to perform a more detailed, time-resolved study, which takes into account possible spectral variations within the 60 ks total exposure. In order to perform this study, we adopted a two-step strategy: we first looked for variations in the spectral shape during the observation, and subdivided it into intervals with constant overall shape, then we performed a complete spectral analysis of each interval. We describe the details of this procedure in the next sections.

5. TIME-RESOLVED SPECTRAL ANALYSIS

The simple analysis performed in R05A and summarized above shows that the primary emission of NGC 1365 is absorbed at energies below 2–3 keV by a column density $N_H \sim 2 \times 10^{23}$ cm^{-2}. Since we are interested in detecting absorption variations, we analyzed the light curves of a hardness ratio HR defined as the ratio between the 2 and 5 keV flux and the 7–10 keV flux. The 2–5 keV spectral interval is where the photoelectric cutoff causes the strongest changes in response to column density variations. The second interval is at energies well above the cutoff, and is not dependent on small N_H variations. The HR light curve is therefore optimized to detect N_H variations, while it is insensitive to intrinsic flux variations.[11] We note that a variation of the spectral shape of the primary continuum would also imply a variation of HR. Therefore, changes in HR do not have a strictly unique interpretation. However, this step does divide the total exposure into intervals with constant spectral shape, which we then analyze separately. The HR light curve is shown in Figure 3. A clear variability is detected, with HR lower (i.e., harder spectrum) in the central ∼20 ks. The total 2–10 keV light curve, also plotted in Figure 3, shows that on average the HR and total flux light curves are correlated. The flux light curve also shows variability on timescales shorter that those investigated with the HR light curve. For such short variations, a detailed spectral analysis is not possible. In the following we will only investigate the variations well detected in the HR light curve. We therefore extracted the spectra from three ∼20 ks intervals, as indicated in Figure 3.

We stress that this approach to spectral analysis is not an ad hoc procedure to search for N_H variations. Indeed, regardless of the physical reason for the observed variations, a time-resolved spectral analysis is needed in order to correctly estimate the parameters of the continuum component. For example, adding states with different intrinsic continuum slopes would introduce artificial curvatures in the spectrum, which could be misrepresented with reflection components and/or broad emission features. Therefore, our method can be considered a generalization of the standard time-averaged spectral analysis.

5.1. Independent Spectral Fits of Each Interval

The spectra extracted from the three time intervals of Figure 3 are plotted in Figure 4. From a visual inspection of these plots we immediately note that the hardness ratio changes in Figure 3 are due to a decrease of the ∼ 2.5–6 keV flux in the second interval, while the three spectra are constant at higher energy. This kind of variation is suggestive of a column density variation, which only affects the energy range around the cutoff, rather than a change in the spectral shape of the intrinsic emission. In order to check this qualitative analysis, we performed a complete spectral analysis of each interval, using the best-fit model of the complete observation as a baseline. At first we left all the parameters free, except for the soft thermal component, which is constant within <3% in all intervals, and is known to be emitted by an extended component on a kiloparsec scale, resolved by *Chandra* observations (R05B).

The results are summarized in Tables 2 and 3, together with the best-fit parameters obtained in the time-integrated fit. As already mentioned at the beginning of the section, in all fits the relativistically broadened iron line is included, and is strongly

[11] This is not strictly true if a constant reflection component is also present. However, the contribution of this component to the observed flux is at the level of a few percent, therefore the effect on HR is expected to be small.

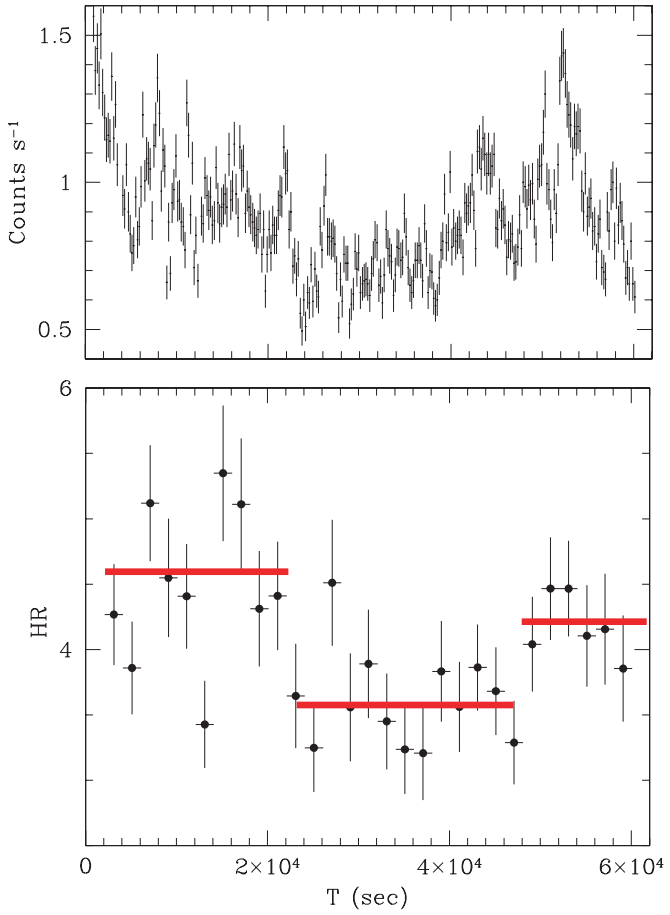

Figure 3. Upper panel: 2–10 keV light curve of the AGN in NGC 1365 (bin size 100 s). Lower panel: hardness ratio HR light curve $F(2–5)/F(7–10)$ (bin size 2000 s). The horizontal lines show the intervals chosen for the time-resolved spectral analysis.

(A color version of this figure is available in the online journal.)

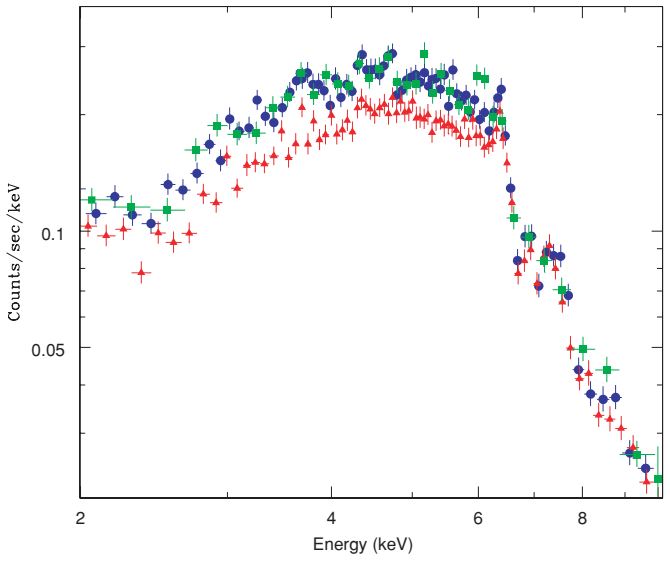

Figure 4. Spectra obtained from the three time intervals shown in Figure 3. The spectra from the first and third intervals (blue circles and green squares) are equal within the errors. The second spectrum (red triangles) is significantly different below ∼6 keV and compatible with the others at higher energies. Only PN data are plotted.

(A color version of this figure is available in the online journal.)

requested by the spectral fit of both the total observation and each of the three intervals. In all cases, a relativistic disk profile around a maximally rotating black hole is preferred to both a simple Gaussian model and a relativistic profile for a nonrotating black hole.

The only continuum parameter varying significantly is the absorbing column density N_H, which changes by $\sim 3\times10^{22}$ cm^{-2} ($\sim$ 20%). The continuum slopes and normalizations are constant within the errors. We plot in Figure 5 the best-fit values of these three parameters. The parameters related to the absorption system at 6.7–8.3 keV and the broad iron line feature also remain constant within the errors, as well as the flux of the narrow iron emission line. Moreover, the fluxes of the cold reflection components (continuum and narrow iron line) are compatible with the values measured in all the previous X-ray observations of NGC 1365.

5.2. Spectral Fits with Constant Continuum

The best-fit models of the three intervals demonstrate that the observed hardness ratio variations are due to changes of column density along the line of sight. We therefore repeated the analysis fitting the three intervals simultaneously, forcing all the parameters except the column density to have the same value in each interval. The results of this new fit are completely compatible with those shown in Table 2, with a factor ∼2 decrease of the uncertainties on the best-fit values of the column densities: $N_H(1) = 14.9^{+0.2}_{-0.2} \times 10^{22}$ cm^{-2}, $N_H(2) = 19.4^{+0.2}_{-0.3} \times 10^{22}$ cm^{-2}, $N_H(3) = 14.7^{+0.3}_{-0.3} \times 10^{22}$ cm^{-2}. Based on these results, we conclude that the statistical significances of the column density variations are at the level of $\sim 20\sigma$ between the first and second intervals, and between the second and third intervals, while the N_H values are equal within the errors in the first and third interval.

The best-fit models obtained here have been used as starting points for the analysis of the two main subjects of this work: the column density variability on even shorter timescales, and the broad emission feature. We discuss these two points in the next two subsections.

5.3. Analysis of Column Density Variations

The obvious physical scenario reproducing the variability found in the spectral fits to the individual intervals is that of a cloud crossing the line of sight to the X-ray source. If this is the case, a more physical model can easily be tested: instead of a single variable column density, the observed variations should be reproduced by a constant column density covering the whole source, plus a second absorber with constant column density but a variable covering factor.

Moreover, the constancy of the continuum component on the timescales of the three intervals (∼20 ks each) suggests that the primary continuum remains constant during the whole observation at all timescales. It is highly unlikely that significant variations of the primary emission happened on timescales shorter than 20 ks, since this would require that the average of these variations is almost exactly (within the measurement errors, which are a few percent for the primary emission component, Table 2) the same in all the three intervals. Therefore, it is safe to assume a constant primary emission at all timescales, so that an analysis of an even shorter timescale becomes possible.

We then performed a new spectral fitting, modifying two key aspects of our analysis.

Table 2
NGC 1365: Time-resolved Spectral Fit—Continuum components

OBS	Γ	N_H[a]	A[b]	R_{COLD}[c]	R_{ION}[c]	F(Fe)[d]	χ_r^2	N_H[e]
TOTAL	$2.56^{+0.07}_{-0.10}$	$15.4^{+0.3}_{-0.2}$	$2.36^{+0.03}_{-0.15}$	$0.5^{+0.3}_{-0.2}$	$0.7^{+0.2}_{-0.2}$	$1.57^{+0.11}_{-0.37}$	1.08	
INT 1	$2.56^{+0.05}_{-0.03}$	$14.8^{+0.4}_{-0.4}$	$2.61^{+0.21}_{-0.32}$	$0.5^{+0.3}_{-0.3}$	$0.4^{+0.3}_{-0.3}$	$1.59^{+0.44}_{-0.28}$	0.98	14.9 ± 0.2
INT 2	$2.57^{+0.05}_{-0.04}$	$18.8^{+0.5}_{-0.3}$	$2.38^{+0.19}_{-0.05}$	$0.4^{+0.3}_{-0.3}$	$0.5^{+0.4}_{-0.2}$	$1.51^{+0.34}_{-0.28}$	0.95	$19.4^{+0.3}_{-0.2}$
INT 3	$2.57^{+0.03}_{-0.03}$	$14.6^{+0.5}_{-0.5}$	$2.77^{+0.23}_{-0.54}$	$0.5^{+0.4}_{-0.4}$	$0.4^{+0.4}_{-0.3}$	<1.3	1.03	14.7 ± 0.3

Notes.
[a] Absorbing column density, in units of 10^{22} cm^{-2}.
[b] Continuum normalization at 1 keV in units of 10^{-2} photons cm^{-2} s^{-1} keV^{-1}.
[c] Ratio between the normalizations of the reflected and primary components.
[d] Normalization of the narrow iron emission line, in units of 10^{-2} photons cm^{-2} s^{-1} keV^{-1}.
[e] N_H values obtained by fitting the three intervals with a constant continuum, as discussed in Section 5.2.

Table 3
NGC 1365—Time-resolved Spectral Fit: Iron Lines Parameters

OBS	E_N[a]	F_N[b]	EW$_N$[c]	E_B[a]	F_B[b]	EW$_B$[c]	R_{IN}[d]	R_{OUT}[d]	$\Delta\chi^2$(S)[e]	$\Delta\chi^2$(G)[e]
TOT	$6.41^{+0.04}_{-0.03}$	$1.57^{+0.11}_{-0.37}$	77^{+5}_{-16}	$6.58^{+0.09}_{-0.06}$	$17.0^{+1.3}_{-2.5}$	535^{+40}_{-80}	$4.5^{+0.3}_{-0.2}$	>120	30	25
INT 1	$6.41^{+0.04}_{-0.04}$	$1.59^{+0.44}_{-0.28}$	71^{+28}_{-13}	$6.58^{+0.08}_{-0.08}$	$16.9^{+2.1}_{-2.3}$	485^{+60}_{-65}	$4.5^{+0.8}_{-1.2}$	>45	30	26
INT 2	$6.41^{+0.03}_{-0.04}$	$1.51^{+0.34}_{-0.28}$	77^{+17}_{-14}	$6.58^{+0.06}_{-0.07}$	$14.5^{+4.0}_{-3.5}$	326^{+90}_{-80}	<3.4	>25	15	6
INT 3	$6.41^{+0.08}_{-0.12}$	<1.3	< 56	$6.58^{+0.14}_{-0.09}$	$16.9^{+1.7}_{-2.2}$	470^{+50}_{-60}	$3.2^{+2.4}_{-0.5}$	>20	18	16

Notes.
[a] Line peak energy, in keV.
[b] Normalizations of the narrow (subscript N) and broad (subscript B) emission lines, in units of 10^{-5} keV s^{-1} cm^{-2} keV^{-1}.
[c] Equivalent width of the broad (B) and narrow (N) emission lines, in eV.
[d] Inner and outer radii of the broad-line emitting region, in units of gravitational radii.
[e] χ^2 increase after replacing the rotating black hole disk line with a nonrotating black hole disk component (S) and a Gaussian line (G). The Gaussian line peak energy was left free, with best-fit values in the range 5.8–6 keV.

1. We used a model with a constant continuum, absorbed by a constant column density N_H(TOT) plus a partial-covering component, with a constant column density N_H(PC) and a variable covering factor $C(t)$.
2. We divided the 60 ks observation into 10 intervals of 6 ks each, and fitted them simultaneously with the above model. All the model components are required to have the same values in all the intervals, except for the partial covering $C(t)$.

The final results for the column density are $N_H(\mathrm{PC}) = 34.8^{+4.6}_{-1.4} \times 10^{22}$ cm^{-2} and $N_H(\mathrm{TOT}) = 12.3^{+0.1}_{-0.2} \times 10^{22}$ cm^{-2}, while the results for the covering fraction C are shown in Figure 6. The variations of C are highly significant and follow the expected pattern for an eclipsing cloud. All the other parameters remain compatible within the errors with those shown in Table 2.

We note that the amount of information contained in Figure 6 is much higher than in Figure 5: our time-resolved spectral analysis resolves a complete transit of a cloud in front of the X-ray source. The precise measurement of the crossing time allows us to put stringent limits on the dimensions of the X-ray source and the obscuring cloud, and on the distance of the cloud from the central black hole. We will discuss this issue in detail in Section 6.

Since this model, obtained through the steps discussed above, is our final "best interpretation" of the time and spectral behavior of NGC 1365, we report all the relevant fit parameters in Table 4 and we show the main components in Figure 7.

The relatively low errors on the single values of the partial-covering parameter are obviously dependent on our choice of adopting a constant continuum. Since the analysis of the three long intervals presented in Section 5.1 shows that the continuum

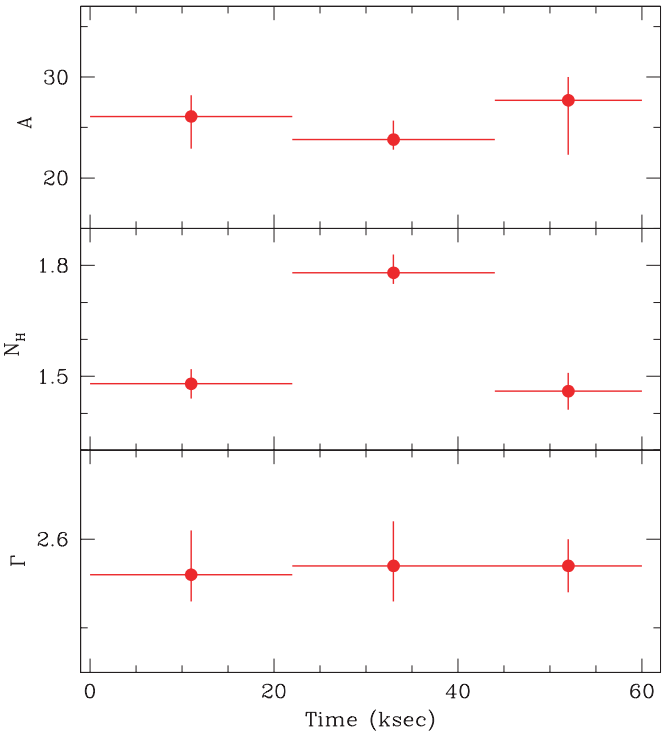

Figure 5. Results of the analysis of the spectra obtained from the three time intervals shown in Figure 3. Upper panel: continuum normalization at 1 keV, in units of 10^{-3} keV s^{-1} cm^{-2} keV^{-1}. Central panel: N_H, in units of 10^{23} cm^{-2}. Lower panel: spectral slope Γ of the primary continuum emission.
(A color version of this figure is available in the online journal.)

remains constant with a maximum statistical uncertainty of ∼10%, we repeated our analysis allowing continuum variations

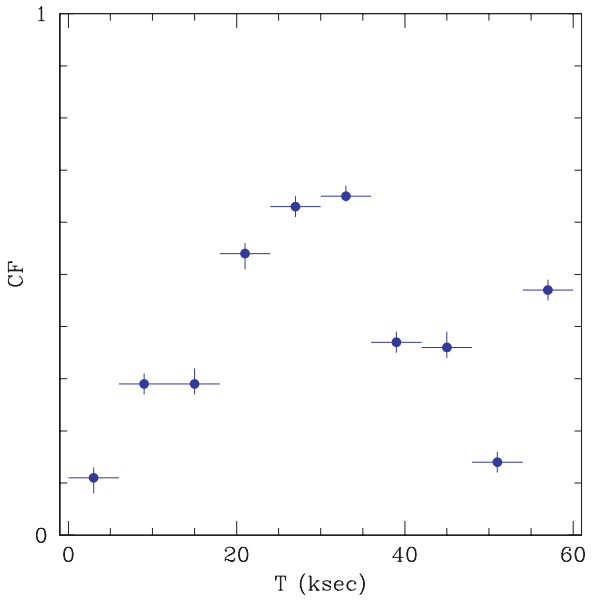

Figure 6. Light curve of the covering fraction of the partial-covering component, obtained by splitting the total exposure into ten 6 ks intervals.
(A color version of this figure is available in the online journal.)

in each interval up to 10%. We found fully consistent values for all the parameters, with the absolute errors on the covering factors higher by ∼30%. This does not affect any of our conclusions.

For completeness, we mention that a similarly good fit is obtained replacing the partial-covering absorber with a single, fully covering absorber with variable column density. The best-fit values obtained in this scenario are all consistent with those shown in Table 4. The N_H best-fit values range from 14 to 20×10^{23} cm^{-2}, with relative errors of a few percent in each interval. We cannot distinguish between these two scenarios on statistical grounds. However, the partial-covering model is the most likely scenario from a physical point of view.

5.4. Analysis of the Broad Iron Feature

A broad emission feature at energies between 4 and 7 keV is clearly present in the spectra (Figure 2) and strongly requested in all our fits (Tables 3 and 4). Even allowing for a variable partial covering, and an ionized reflector, as in the model described in the previous section, the requirement for this feature remains strong: the fit improvement with respect to a narrow component only in our final fit is $\Delta\chi^2 = 205$ with four additional parameters.

We also note that a simple broad Gaussian line model provides a significantly worse fit: $\Delta\chi^2 = 20$, with a best-fit peak energy $E \sim 5.7$ keV. If the peak energy is forced to be within the physically acceptable interval (6.39–6.9 keV) the fit is worse by $\Delta\chi^2 = 160$. Moreover, a model assuming a relativistic profile from a nonrotating black hole also provides a worse fit ($\Delta\chi^2 = 70$).

In order to visualize these results, we plot in Figure 8 the relevant data regarding the broad emission line. A plot of each interval is not easily readable, because the statistics is too low, and the information is hidden in the noise. Therefore, we plot the total residuals to the best fit without the relativistic line component, obtained by adding the residuals of each individual spectrum. For comparison, we also plot the residuals to the best fit *with* the line component and the model components representing the intrinsic (unabsorbed) line and the observed (absorbed) line for the first (least obscured) and fifth (most obscured) intervals. These model lines contain interesting information: they show the non-negligible effects of absorption on the broad line and show the difference between the different phases of the eclipse.

As a further step in order to obtain a physically consistent scenario, we repeated our fits using a relativistic blurring model applied to the whole disk reflection spectrum, i.e., to both the disk emission line and the warm reflection continuum component, assumed to originate from the disk as well. The relativistic blurring has been applied to the disk reflection model of Ross & Fabian (2005) which includes both the reflection continuum and the iron emission line from an ionized disk. This replaces the blurred ionized reflection and the LAOR broad emission line components in our model. All the

Table 4
Partial-covering Model

Continuum	
Γ	$2.49^{+0.01}_{-0.02}$
A[a] (10^{-2} keV cm^{-2} s^{-1} keV^{-1})	$2.75^{+0.03}_{-0.04}$
R_{COLD}[b]	$0.3^{+0.2}_{-0.1}$
R_{ION}[b]	$0.4^{+0.1}_{-0.1}$
Absorption	
N_H(TOT) (10^{22} cm^{-2})	$34.8^{+4.6}_{-1.4}$
N_H(PC) (10^{22} cm^{-2})	$12.3^{+0.1}_{-0.2}$
C_1	$0.11^{+0.02}_{-0.03}$
C_2	$0.28^{+0.02}_{-0.02}$
C_3	$0.51^{+0.01}_{-0.02}$
C_4	$0.59^{+0.02}_{-0.01}$
C_5	$0.62^{+0.01}_{-0.02}$
C_6	$0.65^{+0.01}_{-0.02}$
C_7	$0.37^{+0.02}_{-0.02}$
C_8	$0.36^{+0.02}_{-0.03}$
C_9	$0.14^{+0.02}_{-0.02}$
C_{10}	$0.47^{+0.02}_{-0.02}$
Emission lines	
E_N[c] (keV)	$6.41^{+0.02}_{-0.02}$
F_N[c] (10^{-5} keV cm^{-2} s^{-1} keV^{-1})	$1.8^{+0.2}_{-0.3}$
EW$_N$[c] (eV)	75^{+10}_{-8}
E_B[d] (keV)	$6.68^{+0.03}_{-0.03}$
F_B[d] (10^{-4} keV cm^{-2} s^{-1} keV^{-1})	$2.1^{+0.2}_{-0.2}$
EW$_B$[d] (eV)	340^{+35}_{-35}
R_{IN} (R_G)	$2.7^{+0.2}_{-0.2}$
R_{OUT} (R_G)	8.5^{+3}_{-1}
θ[e]	24^{+8}_{-4}
q[f]	$4.3^{+0.5}_{-0.4}$
$\Delta\chi^2$(G)[g]	25
$\Delta\chi^2$(S)[g]	70
F(2–10)[h] (10^{-11} erg cm^{-2} s^{-1})	1.24
L(2–10)[i] (10^{42} erg s^{-1})	2.50
χ^2/d.o.f.	2687/2748

Notes.
[a] Normalization at 1 keV of the primary power law component.
[b] Ratio between the normalizations of the reflected and primary components.
[c] Narrow emission line.
[d] Broad emission line.
[e] Disk inclination angle in the broad-line component.
[f] Slope of the disk emissivity profile.
[g] Increase of χ^2 for a Gaussian model (G) or a Schwarzschild model (S) for the broad line. In the Gaussian model the line peak energy is free to vary, and its best fit value is ∼5 keV.
[h] Average observed 2–10 keV flux.
[i] Absorption-corrected 2–10 keV luminosity.

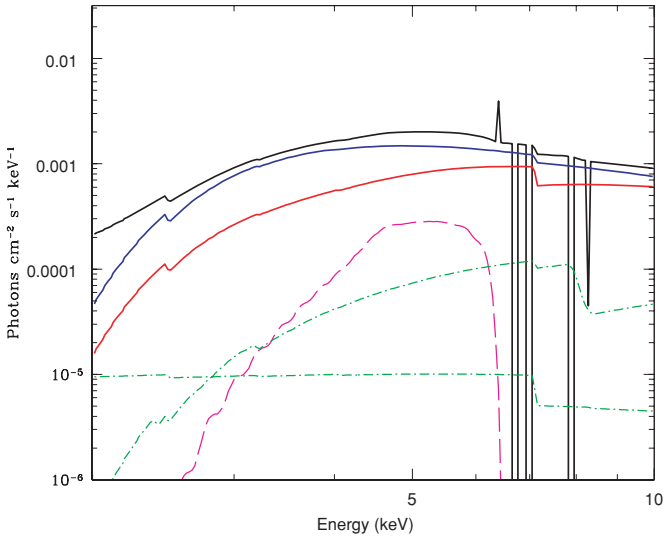

Figure 7. Main components of our final, variable partial-covering model. Upper continuous line (black): total model, including the narrow absorption and emission lines. Bottom continuous lines: absorbed primary power law, for the minimum (blue) and the maximum (red) covering factor in Table 4. Dashed line (magenta): relativistic iron emission line. Dot-dashed lines (green): ionized and neutral reflection components.

(A color version of this figure is available in the online journal.)

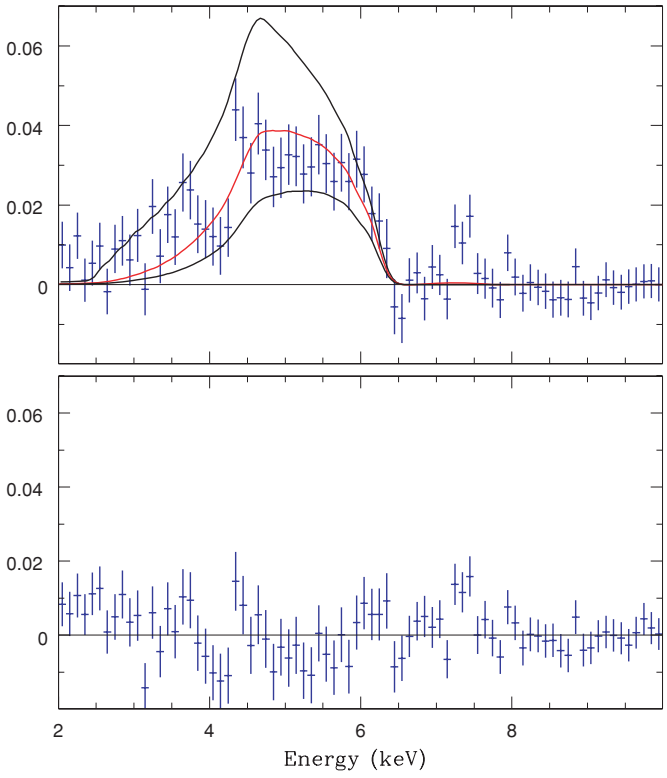

Figure 8. Upper panel: ratio to the best-fit model without the broad iron line components. The profile has been obtained by adding the residuals of all the spectra obtained from the 10 intervals in which we split the observation. The black, highest line shows the best-fit unabsorbed line. The two lower lines show the observed (i.e., absorbed) line profiles for the first and fifth intervals, where the covering factor of the absorbing cloud was minimum and maximum, respectively. Lower panel: as above, residuals to the complete best-fit model, including the relativistic iron line.

(A color version of this figure is available in the online journal.)

other components are unchanged with respect to the previous subsection.

The main results are the following.

1. The overall fit is similar to the standard partial covering one shown in Table 4 (χ^2/dof = 2700/2748).
2. The best-fit values for the inner and outer radii of the emitting region are $R_{\rm IN} = 5^{+1}_{-1} R_G$ and $R_{\rm OUT} = 14^{+8}_{-4} R_G$.
3. The best-fit ionization parameter is $U = 1.1^{+0.1}_{-0.3} \times 10^3$ erg cm s^{-1}.
4. The iron abundance is $2.8^{+0.2}_{-0.3}$ with respect to standard solar abundances.
5. The best-fit values of the other parameters are compatible with those found in the simpler partial-covering fit, as shown in Table 4.

We note that in the previous model, while the line emitting region parameters (emissivity profile, inner and outer radius, inclination angle) are well determined by the fit, the analogous parameters for the continuum components are not significantly constrained, as already noted in Section 2. Since we now apply the relativistic blurring to a line+continuum model, it is natural to obtain parameters in agreement with those of the LAOR model in the previous fit. The main advantage in this new model is a consistent treatment of the relative strength of the line and continuum components, which allows an estimate of the iron abundance, not possible in the "standard" partial-covering model of Table 3.

5.5. *Results from other* XMM-Newton *Observations*

Two more *XMM-Newton* observations of NGC 1365 have been performed since 2004: a further 60 ks observation performed approximately six months after the one presented here, in 2004 July, and a "long look" consisting of three consecutive orbits (∼370 ks total) in 2007. Here we report the results of the analysis of both. We just quickly summarize the results on the "long look," which are presented in another paper (Risaliti et al. 2009), while we give some more details on the analysis of the second 60 ks observations, which is not presented elsewhere.

1. *The long look*. An *XMM-Newton* 3 orbit monitoring of NGC 1365 was performed in 2007 May. During this long observation the source was mostly in a Compton-thick, reflection-dominated state. However, during the second orbit we observed a "hole" in the Compton-thick absorber, which revealed the intrinsic X-ray source. A detailed analysis of the emission and absorption components, as the one presented here, is not possible for this observation, due to the high residual column density in the Compton-thin state ($N_H \sim 9 \times 20^{23}$ cm^{-2}). Therefore, a much simpler model has been adopted, without the broad line and absorption line components. However, the duration of the "anti-eclipse" allowed a precise determination of the size of the X-ray source and of the distance of the Compton-thick clouds. These results, presented in Risaliti et al. (2009), are complementary to our current analysis of the Compton-thin absorber, in order to obtain a complete view of the circumnuclear absorber/reflector of NGC 1365.
2. *The 2004 July 60 ks observation*. A further 60 ks *XMM-Newton* observation (hereafter OBS 2) was performed in 2004 July, six months after the observation discussed in this paper (hereafter OBS 1). We applied to these data the same analysis described in the previous sections, starting from a fit of the whole observation and then searching for possible spectral variations. The main relevant results of this analysis are the following.

a) The light curves of both the total emission and the hardness ratio do not show significant variations. As a consequence, we only analyzed the spectrum obtained from the whole observation.

b) The source is in a Compton-thin state with an equivalent column density $N_H \sim 3 \times 10^{23}$ cm^{-2} (see below for more details on the structure of the absorber). This implies that the red tail of the broad iron emission line is heavily suppressed by absorption. We included a relativistic broad line in our model, and we found that this component is perfectly consistent with that found in the OBS 1 spectrum. However, the uncertainties on the line parameters are too high to add additional evidence to the case of the broad relativistic line. Therefore, we will not discuss this component further.

The continuum emission can be fitted equally well with two different models: (1) a fully obscured power law with $\Gamma \sim 2.2$ and $N_H \sim 3 \times 10^{23}$ cm^{-2} (this is the model presented in R05A) and (2) an obscured power law with $\Gamma \sim 2.5$ and $N_H \sim 2.5 \times 10^{23}$ cm^{-2} partially obscured by a second absorber, with $N_H \sim 2.5 \times 10^{23}$ cm^{-2}, and covering fraction $C = 70\% \pm 10\%$. The two fits are statistically equivalent ($\chi^2_{\rm red} = 1.01$ for both). This means that the inclusion of the second, partially covering absorber does not improve the fit from a purely statistical point of view. However, the best-fit continuum parameters make the partial-covering model particularly interesting: not only the photon index is the same as in OBS 1, but the power-law normalization is also perfectly consistent ($A = 2.5^{+0.3}_{-0.4} \times 10^{-2}$ erg cm^{-2} s^{-1} keV^{-1}). All the other model components (reflection continuum, emission, and absorption lines) are also consistent with the OBS 1 parameters shown in Table 4. Since all the fitting parameters, and in particular the slope and normalization of the primary continuum, are left free to vary, these results suggest a scenario with a constant continuum on timescales of months, and with the absorber as the only variable component. Obviously, we cannot exclude that the simpler, one-absorber model is the correct one, and that the constancy of the continuum parameters assuming the partial-covering model is due to a "cosmic conspiracy." Future studies, involving the analysis of all the available X-ray observations of NGC 1365 through partial-covering models, will clarify this interesting issue. However, in the present paper we consider the partial-covering model as the most likely from a physical point of view.

6. DISCUSSION: THE VARIABLE ABSORBER

The obscured AGN in NGC 1365 has several unique properties, which make it the best laboratory to investigate the structure of the obscuring/reflecting medium (both disk and circumnuclear gas) found so far among obscured AGNs. In the previous section, we presented a detailed time-resolved spectral analysis of a 60 ks *XMM-Newton* observation, which showed a clear variation of obscuration due to a cloud with $N_H \sim 3 \times 10^{23}$ cm^{-2} crossing the line of sight.

The partial eclipse of the X-ray source allows a direct estimate of the sizes of the X-ray emitting region and of the obscuring cloud, and of the distance between them. From the analysis of Figure 5 and Table 4 we note that the time profile of the variation cannnot have a flat top longer than about 12 ks, being the values of C_5 and C_6 consistent, while $C_5 > C_4$ and $C_6 > C_7$. This suggests that the covering cloud is about of the same size as the X-ray source. If the cloud were much bigger than the source, it should cover a roughly constant fraction of the source in the central phase of the eclipse, leading to a plateau in the covering factor light curve. On the other hand, the cloud section cannot be smaller than ∼65% of the source size to achieve the maximum covering factor ($C_6 \sim 65\%$ in Table 4). A more detailed study of the shape of the obscuring cloud and of the emitting region is not possible with the available data. A higher S/N detection of an eclipse could in principle provide strong constraints on the geometry. This could be possible with future X-ray observatories, or, even using currently available instrumentation, if an eclipse with a higher N_H cloud and/or with a complete obscuration of the central source is observed. This would greatly increase the precision of the measurements of the covering factors, thus allowing a more detailed investigation of the shapes of cloud and source.

In order to estimate the size of the X-ray emitting region, we assume a spherical, homogeneous cloud with diameter $D_{\rm C}$, column density N_H, and number density $n = N_H/D_{\rm C}$, at a distance R from the central black hole, moving with Keplerian velocity $V_{\rm K} = \sqrt{GM_{\rm BH}/R}$. Since the observed eclipse is almost complete, we assume that the linear size of the X-ray source is $D_{\rm S} \sim V_{\rm K} \times T$, where T is the measured occultation time, which in our case is ∼25 ks. An estimate of $V_{\rm K}$ can be obtained from three different arguments.

1. *Limits on the ionization parameter of the obscuring cloud.* The observed absorption variations require that the obscuring cloud is not overionized. We require $U < U_{\rm MAX} = 20$ erg cm s^{-1} (see Risaliti et al. 2007, 2009 for details). Using this limit, and the geometrical condition that the cloud must be of the same size of the X-ray source (see discussion above), after straightforward algebra we obtain $R > (GM_{\rm BH})^{1/5}[T \times L_{\rm X}/(U_{\rm max}N_H)]^{2/5}$. The black hole mass can be estimated using the mass–bulge luminosity, mass–bulge velocity dispersion, and mass–Hβ width relationships. The available estimates are $\log(M_{\rm BH}/M_\odot) = 7.3 \pm 0.4(0.3)$ from the $M_{\rm BH}$–bulge velocity dispersion correlation (Oliva et al. 1995; Ferrarese et al. 2006) and $\log(M_{\rm BH}/M_\odot) = 7.8 \pm 0.4(0.3)$ from the relation between $M_{\rm BH}$ and the K magnitude of the host bulge (Dong & De Robertis 2006; Marconi & Hunt 2003), where the errors include statistical and systematic effects and the number in brackets refer to the statistical dispersion of the correlation. We note that the $M_{\rm BH}$–bulge luminosity correlation likely overestimates $M_{\rm BH}$ in the case of NGC 1365, due to the high starburst contribution to the bulge luminosity. A much smaller estimate (but still compatible with the $M_{\rm BH}$–velocity dispersion relation) is obtained from the width of Hβ: assuming FWHM(Hβ) = 1900 km s^{-1}, as measured by Schulz et al. (1999), and the Kaspi et al. (2005) $M_{\rm BH}$–FWHM(Hβ) relation, we obtain $M_{\rm BH} \sim 2 \times 10^6\ M_\odot$. Adopting $L_{\rm X} = 1.9 \times 10^{42}$ erg s^{-1} cm^{-2} (obtained by extrapolating our absorption-corrected luminosity to the 1–100 keV band), and the measured N_H and T, we obtain $R > 2 \times 10^{15} M_7^{1/5}$ cm, $V_{\rm K} < 7,600 M_7^{3/10}$ km s^{-1}, and $D_{\rm S} < 1.9 \times 10^{13} M_7^{3/10}$ cm, where $M_7 = M_{\rm BH}/(10^7\ M_\odot)$. This size corresponds to 6 gravitational radii for $M_{\rm BH} = 10^7\ M_\odot$ and 20 gravitational radii for $M_{\rm BH} = 2 \times 10^6\ M_\odot$.
2. *Geometrical limits.* A purely geometrical limit comes from the requirement that the cloud and the X-ray source are physically separated, i.e., that the distances from their centers are $R > R_{\rm min} = (D_{\rm C} + D_{\rm S})/2 \sim D_{\rm S}$. From $D_{\rm S} = V_{\rm K} \times T$ we obtain $R_{\rm min} = (GM_{\rm BH})^{1/3} T^{2/3} =$

$9.4 \times 10^{13} M_7^{1/3}$ cm, $D_S < R_{min}$, and $V_K < 38{,}000 M_7^{1/3}$ km s^{-1}. These values describe an unlikely geometry, with the edge of the cloud touching the edge of the X-ray source. However, they are interesting because they represent strong limits to the source size. We note that even in this extreme configuration the size of the emitting region is only ∼30 gravitational radii for $M_{BH} = 10^7\ M_\odot$.

3. *Limits from the width of the emission line*. We can reasonably assume that the variable component of the obscuring gas is the same responsible for the cold reflection component present in our best-fit models, and best seen in the previous observations of NGC 1365 which caught the source in a Compton-thick, reflection-dominated state. We can therefore use the width of the "narrow" iron emission line to estimate the velocity of the obscuring clouds, under the assumption that the thick clouds (responsible for the bulk of the iron emission line) and the thin ones are at about the same distance from the central source. We note that a small contribution to the observed narrow emission line can be given by the constant N_H component, for which no constraints on the distance based on our arguments are possible. However, since the column density of this component is only of the order of 10^{23} cm^{-2}, we expect only a minor contribution to the observed iron line flux. The narrow iron line is resolved in the "long-look" observation presented in Risaliti et al. (2009), which gives $V_{Fe} = 2^{+1}_{-1} \times 10^3$ km s^{-1}. Considering that the measured width of the emission line is affected by the projection effects of a distribution of clouds rotating around the central source, while the crossing cloud is moving in the plane of the sky, we obtain $V_K = 3000$ km s^{-1}, $R \sim 1.5 \pm 0.7 \times 10^{16}$ cm, and $D_S < 7.5 \times 10^{12}$ cm $= 2.5\ M_7^{-1} R_G$. This low value suggests that the correct value for the black hole mass is not higher than $\log(M_{BH}/M_\odot) = 6.5$, in agreement with the M_{BH}–FWHM(Hβ) correlation.

These results are complemented by the analysis of the 60 ks 2004 July observation, summarized in Section 5.5 and the 370 ks "long look" (Risaliti et al. 2009).

The 2004 July observation shows that the Compton-thin absorber is not only made of clouds of the same size of the X-ray source, as observed in the 2004 January observation. In particular, the constancy of the covering fraction C in the 2004 July observation implies that the covering cloud is significantly larger than the X-ray source. Assuming a cloud with radius D_C, covering at most ∼60% of the source, in order to have C constant within 15%, as observed (Section 5.5), we must have $D_C > 3D_S$. An alternative way to obtain the same constancy is by assuming a distance of the obscuring cloud from the center ∼10 times larger than in the 2004 January observation. We consider this possibility unlikely, though still possible.

The "long look" provides complementary information of the Compton-thick phase of the absorber, showing that clouds with $N_H > 10^{24}$ cm^{-2} are also present, at about the same distance from the central source as the thin clouds. The persistence of the Compton-thick state of >2 days also suggests that the thick clouds are significantly larger than the X-ray source (even if a superposition of several, smaller thick clouds cannot be excluded, see Risaliti et al. 2009 for details).

Summarizing, the available *XMM-Newton* observations of NGC 1365 suggest that the obscuring medium is made of clouds with column densities from a few 10^{23} to $> 10^{24}$ cm^{-2}, and sizes form about that of the X-ray source to several times larger.

7. DISCUSSION: THE BROAD IRON LINE

The broad iron line found in our observation is best fitted by a relativistically smeared profile, due to a rotating black hole. The significance of the broad line is one of the highest ever found among AGNs.

The fit with a rotating black hole is preferred with respect to the pure Schwarzschild case. However, the relatively large inner radius obtained in our fits ($R_{IN} \sim 3$ and $R_{IN} \sim 4$–6 in the two final fits discussed above) suggests that a maximally rotating black hole disk is not really requested by our data. More detailed models of the line profiles (e.g., Dovčiak et al. 2004) show that solutions with a maximally rotating Kerr profile and an inner radius $R_{IN} \sim 4$ are equivalent (with our data quality) to solutions starting from the least stable orbit and with an angular momentum parameter $a \sim 0.6$. Since we cannot resolve this degeneracy, we conservatively conclude that our data suggest that the black hole is rotating with $a > 0.6$.

The detailed fits performed in order to study the variability of the circumnuclear absorber are a strong check on the significance of this feature. Indeed, our models contain several components which could mimic a relativistic line: a cold and an ionized reflection component, and a variable partial covering. In particular, the variable partial covering introduces a curvature in the integrated continuum which could be interpreted as due to the red tail of the relativistic line. It is quite instructive to compare the line parameters obtained from the total 60 ks observation (Table 3) with those obtained from the time-resolved fit (Table 4).

1. The (absorption-corrected) equivalent width of the broad line in the former is significantly higher than in our final best fit including partial covering. Its value is higher than the typical equivalent width measured in Seyfert 1s by a factor of at least 3. Such high values are suspicious, and are the indication of a possible incorrect estimate of the continuum level in the global fit, due to not properly considering the spectral curvature due to the N_H variations.
2. The parameter errors are significantly larger. In particular, the outer radius of the emitting line is not well constrained, and the uncertainty on the line flux is of the order of 20%, a factor ∼3 higher than in our final fit.

   All the problems present in the fit of the whole observation are solved with the time-resolved approach. Our final best fit still requires a relativistic iron line, and the correct estimate of the variable continuum level provides a more reasonable equivalent width (Table 4) and a better determination of the line parameters.

Overall, the variable partial-covering models (the standard one with separate iron and reflection components, and the Ross & Fabian 2005 one where the line and continuum reflections are treated self-consistently) provide a complete view of the X-ray emitting region and the reflecting/absorbing medium.

1. The equivalent width of the line is higher than 300 eV, among the highest values measured for these features in nearby AGNs (e.g., Miller 2007). This high value is physically explained by the high iron metallicity estimated in the final line+continuum reflection model (Z(Fe) ∼ 3).
2. The outer radius of the line emitting region, estimated both from the relativistic line component in the standard partial-covering model and from the relativistic blurring component in the *kdblur* model, is relatively small

($R_{\rm OUT} < 15R_G$). This parameter is interesting when compared with the size of the X-ray source: both the eclipses observed during the *Chandra* campaign and the *XMM-Newton* long look, and the occultation event occurred during this observation suggests that the X-ray source is confined within a few gravitational radii from the central black hole. The upper limit on the outer radius of the iron line is a further, completely independent indication supporting this scenario.

3. In addition to the broad iron line and the extreme variability behavior, the AGN in NGC 1365 shows another peculiar property, not analyzed here (but included in all the models): the system of four iron absorption lines in the 6.7–8.3 keV interval, discussed in detail in R05A. The main results of the analysis of those lines are that they are due to a highly ionized ($U > 1000$ erg cm s^{-1}) absorber, with a column density of a few 10^{23} cm^{-2}. The physical properties of this gas strongly suggest that it is located very close to the central source (at $\sim$50–100R_G), i.e., "inside" the clumpy cold absorber. These properties strongly suggest that this gas is the Compton-thin, lower density extension at larger radii of the warm, Compton-thick component responsible for the iron emission line and the highly ionized reflection. In this scenario, the expected emission of this component would be a weak scattering component, not distinguishable from the direct continuum emission in the spectral fit.
4. The high equivalent width of the four absorption lines, never observed in other similar AGNs, suggests some peculiar property of this absorber, not present with the same intensity in other sources. The most obvious reason for the presence of these strong lines, beside a particularly high column density and high ionization warm absorber (see above), is an overabundance of iron with respect to the other heavy elements. This would easily explain the unusual strength of the observed lines: a factor of $\sim$a few enhancement of iron in NGC 1365 would justify the lack of similar detections in other bright AGNs. This scenario is now strongly supported by our measurement of the equivalent width of the broad emission line, a factor $\sim$3 higher than the average value measured in local AGNs, and by the best-fit iron abundance in the relativistic blurring partial-covering model, Z(Fe) $\sim$3. At completely different scales, an iron overabundance is also suggested by the analysis of the *XMM-Newton* RGS high resolution soft X-ray spectrum of the diffuse emission (Guainazzi & Bianchi 2007; Guainazzi et al. 2009). In order to further check the case for an iron overabundance, we also fitted the cold absorber with a variable iron abundance. However, we were not able to obtain strong constraints for this extra parameter, which can be anyway consistent with an iron overabundance of $\sim$3 without any significant change in the fits presented in the previous sections. Summarizing, the available observations strongly suggest the presence of an iron overabundance at all scales from $\sim$1 kpc down to a few gravitational radii form the central black hole.

Despite the consistency of the above scenario, the interpretation of the broad 4–6 keV feature as a relativistic iron line is not unique. In particular, it has been proven that the same profile can be reproduced by a combination of partially ionized variable absorbers (Miller et al. 2008). Here we do not fully analyze this scenario, but we only note two important aspects. (1) In principle, it is not possible to rule out an extra continuum plus warm absorber(s) component with the same profile as our emission line, if multiple components with free ionization states are allowed. (2) None of our absorbing/reflecting components seem to introduce alterations in the continuum shape that have not been included in our fits. In particular, we used the XSTAR code in XSPEC to simulate the possible contribution of the warm absorber associated with the Fe XXV and Fe XXVI absorption lines. The result is that a gas with an ionization parameter as high as the one measured from the lines' peak energies and flux ratios (R05A) does not significantly affect the continuum profile. In order to produce significant spectral curvature, a lower ionization state is required, which would produce a detectable set of absorption structures around 6.5–6.6 keV, none of which have even been detected in NGC 1365.

8. CONCLUSIONS

We have presented a complete, time-resolved spectral analysis of a 60 ks *XMM-Newton* observation of the AGN in NGC 1365. The source was on average in a high flux, relatively low-absorption ($N_H \sim 1.5 \times 10^{23}$ cm^{-2}) state. An analysis of the hardness ratio light curve revealed a strong spectral variability during the observation, which we interpret as due to a cloud with $N_H = 3.5 \times 10^{23}$ cm^{-2} crossing the line of sight in $\sim$25 ks, with a maximum coverage of the X-ray emitting region of about 65%.

The analysis also revealed the presence of a strong, broad iron emission line, best fitted with a relativistic profile due to a rotating black hole. The significance of this line has been confirmed allowing for neutral and ionized reflection, and for time variable partial absorption. The best-fit outer radius of this line is of the order of $\sim 10R_G$. This is an indication that the X-ray emitting region is concentrated in the inner part of the accretion disk, in agreement with the results of the variability analysis: the parameters of the observed eclipse suggest that the X-ray source is confined within $< 20R_G$ from the central black hole.

The main conclusions of our study are the following.

1. The partial eclipse detected in this observation demonstrates that the obscuring material consists (at least in part) of clouds with column density of the order of a few 10^{23} cm^{-2}. Assuming that these clouds rotate with Keplerian velocity around the central source, we obtain a distance from the central black hole of the order of 10^{16} cm. The inferred cloud density is a few 10^{10} cm^{-3}. These are typical values for clouds emitting the high ionization broad emission lines in the optical/UV of type 1 AGNs. Therefore, we identify the variable circumnuclear absorber as due to a BLR cloud.
2. The inferred size of the X-ray emitting region is of the order of 10^{13} cm. Assuming the black hole mass value obtained from the standard relations between black hole mass and bulge luminosity/velocity dispersion, this corresponds to $\sim$ 10–25 gravitational radii.
3. We fitted a global model for the accretion disk reflection (both line and continuum components) smeared by the general relativistic effects of a rotating black hole, and found a iron overabundance of a factor of $\sim$3. This high value easily explains (*a*) the high significance of our detection, "helped" by the unusually high equivalent width of the broad line and (*b*) the peculiar set of Fe XXV and Fe XXVI absorption lines present in this spectrum (and discussed in a previous paper, R05A), with an optical depth never measured in any other (bright) AGN. With a standard solar iron abundance both features would be barely detectable.

4. By comparing the results of our last, time-resolved spectral analysis with the standard global spectral fit, we note that the parameters relative to these components are significantly different in the two fits, and the uncertainties are much larger in the global fit. In particular, the best-fit line equivalent width is higher in the latter (EW$\sim$500 eV), and the inner and outer radii are poorly constrained. This can be explained if the absorption variations introduce a curvature in the continuum global spectrum, which is incorrectly fitted with an excessively strong and broad emission line. As a consequence, the case of variable partial absorption should always be checked in the spectral analysis of long X-ray observations of AGNs.

The results presented here, together with those from the *Chandra* monitoring campaign (Risaliti et al. 2007) and the *XMM-Newton* long look (Risaliti et al. 2009), provide a detailed view of the circumnuclear absorber, both in the Compton-thin and Compton-thick components.

However, more work is still to be done on the X-ray emission of NGC 1365: indeed, in order to constrain the structure and size of the X-ray emitting region and of the circumnuclear clouds, the "optimal" observation is still missing: a continuous monitoring of a complete eclipse of a low-N_H, Compton-thin state, by a Compton-thick cloud. Such observation would better constrain the properties of the circumnuclear absorber and would offer a unique opportunity to perform an experiment of "accretion disk tomography": at different phases of the eclipse, different regions of the X-ray source would be visible.

Finally, a further ongoing development of our study of the circumnuclear medium of AGNs consists of applying the time-resolved analysis presented here to more sources. Our first choices are the few other known "changing look" AGNs, i.e., sources which were observed in both a Compton-thin and a reflection-dominated state. For one of these objects, UGC 4203 (the "Phoenix Galaxy," Guainazzi 2002), we already obtained a *Chandra* monitoring campaign analogous to that performed on NGC 1365. The (positive) results of these observation will be presented in a future paper.

We are grateful to the referee for helpful comments which significantly improved the clarity of the paper. This work was partially supported by NASA grants G06-7102X and NNX07AR90G.

REFERENCES

Arnaud, K. A. 1996, in ASP Conf. Ser. 101, Astronomical Data Analysis Software and Systems V, ed. George H. Jacoby & Jeannette Barnes (San Francisco, CA: ASP), 17
Bianchi, S., Guainazzi, M., & Chiaberge, M. 2006, A&A, 448, 499
Bianchi, S., Matt, G., Nicastro, F., Porquet, D., & Dubau, J. 2005, MNRAS, 357, 599
Dong, X. Y., & De Robertis, M. M. 2006, AJ, 131, 1236
Dovčiak, M., Bianchi, S., Guainazzi, M., Karas, V., & Matt, G. 2004, MNRAS, 350, 745
Elvis, M., Risaliti, G., Nicastro, F., Miller, J. M., Fiore, F., & Puccetti, S. 2004, ApJ, 615, L25
Fabian, A. C., & Miniutti, G. 2009, in The Kerr Spacetime: Rotating Black Holes in General Relativity, ed. D. L. Wiltshire, M. Visser, & S. M. Scott (Cambridge: Cambridge Univ. Press), 236 (arXiv:astro-ph/0507409)
Fabian, A. C., Rees, M. J., Stella, L., & White, N. E. 1989, MNRAS, 238, 729
Ferrarese, L., et al. 2006, ApJ, 644, L21
Ghisellini, G., Haardt, F., & Matt, G. 1994, MNRAS, 267, 743
Gilli, R., Maiolino, R., Marconi, A., Risaliti, G., Dadina, M., Weaver, K. A., & Colbert, E. J. M. 2000, A&A, 355, 485
Guainazzi, M. 2002, MNRAS, 329, L13
Guainazzi, M., & Bianchi, S. 2007, MNRAS, 374, 1290
Guainazzi, M., Matt, G., Fiore, F., & Perola, G. C. 2002, A&A, 388, 787
Guainazzi, M., et al. 2009, submitted
Iyomoto, N., Makishima, K., Fukazawa, Y., Tashiro, M., & Ishisaki, Y. 1997, PASJ, 49, 425
Kaspi, S., Maoz, D., Netzer, H., Peterson, B. M., Vestergaard, M., & Jannuzi, B. T. 2005, ApJ, 629, 61
Krolik, J. H., & Begelman, M. C. 1988, ApJ, 329, 702
Laor, A. 1991, ApJ, 376, 90
Magdziarz, P., & Zdziarski, A. A. 1995, MNRAS, 273, 837
Marconi, A., & Hunt, L. K. 2003, ApJ, 589, L21
Matt, G., Guainazzi, M., & Maiolino, R. 2003, MNRAS, 342, 422
Miller, J. M. 2007, ARA&A, 45, 441
Miller, L., Turner, T. J., & Reeves, J. N. 2008, A&A, 483, 437
Nandra, K., O'Neill, P. M., George, I. M., & Reeves, J. N. 2007, MNRAS, 382, 194
Oliva, E., Origlia, L., Kotilainen, J. K., & Moorwood, A. F. M. 1995, A&A, 301, 55
Peterson, B. M., & Wandel, A. 2000, ApJ, 540, L13
Puccetti, S., Fiore, F., Risaliti, G., Capalbi, M., Elvis, M., & Nicastro, F. 2007, MNRAS, 377, 607
Risaliti, G. 2002, A&A, 386, 379
Risaliti, G., Bianchi, S., Matt, G., Baldi, A., Elvis, M., Fabbiano, G., & Zezas, A. 2005a, ApJ, 630, L129 (R05A)
Risaliti, G., Elvis, M., Fabbiano, G., Baldi, A., & Zezas, A. 2005b, ApJ, 623, L93 (R05B)
Risaliti, G., Elvis, M., Fabbiano, G., Baldi, A., Zezas, A., & Salvati, M. 2007, ApJ, 659, L111
Risaliti, G., Elvis, M., & Nicastro, F. 2002, ApJ, 571, 234
Risaliti, G., Maiolino, R., & Bassani, L. 2000, A&A, 356, 33
Risaliti, G., et al. 2009, MNRAS, 393, L1
Ross, R. R., & Fabian, A. C. 2005, MNRAS, 358, 211
Schulz, H., Komossa, S., Schmitz, C., & Mücke, A. 1999, A&A, 346, 764
Strüder, L., et al. 2001, A&A, 365, L18
Tanaka, Y., et al. 1995, Nature, 375, 659
Turner, M. J. L., et al. 2001, A&A, 365, L27
Urry, C. M., & Padovani, P. 1995, PASP, 107, 803
Wang, J., Fabbiano, G., Elvis, M., Risaliti, G., Mazzarella, J. M., Howell, J. H., & Lord, S. 2009, ApJ, 694, 718